



Disentangling the Components of the Milky Way

Inferring the Structure of the Milky Way in Phase-Space Using Gaussian Mixture
Modelling with Extreme Deconvolution

A REPORT PRESENTED
BY
RAUNAQ RAI

Departments

Department of Physics (Cavendish Laboratory)
Institute of Astronomy

Degree

MPhil in Data Intensive Science

Supervision

Dr Anke Arentsen



St Edmund's College
University of Cambridge

29th June 2025

Abstract

Contents

1	Introduction	6
1.1	Components of the Milky Way	6
1.2	Metallicity as a Cosmic Clock	6
1.3	Λ CDM: hierarchical growth and a lopsided halo	7
1.4	Accretion versus <i>in-situ</i> disc formation	7
1.5	Origins of very-metal-poor disc candidates	8
1.6	This Work	8
2	Data	9
2.1	Sample construction	9
2.2	Galactocentric Positions and Velocities	9
3	Methodology	12
3.1	Gaussian Mixture Model	12
3.2	Number of Gaussian Components	13
4	Results	14
4.1	Gaussian Mixture Model Fit	14
4.2	Rotational Support and the Onset of Disc Formation	16
4.3	Residual Analysis for Hidden Disc Populations	16
5	Extension analysis	18
5.1	Alpha-element abundance	18
5.2	Data	19
5.3	Gaussian Mixture Model Fit	24
5.4	High alpha Gaussian Mixture Model Fit	25
5.5	Low alpha Gaussian Mixture Model Fit	26
5.6	Comparing the high and low α GMMs	26
6	Discussion	27
7	problems with Zhang et al. [2024]	27
8	Extension direction	27
9	Conclusion	27

List of Figures

- 1 Properties of the final RGB sample after all quality and footprint cuts. *Left*: heliocentric-distance histogram for the whole sample (grey); the subsets with $-3 < [\text{M}/\text{H}] < -1$ and $-3 < [\text{M}/\text{H}] < -2$ are shown in solid red and dashed blue, respectively. *Middle*: density map in Galactocentric cylindrical coordinates. The empty band at low $|Z|$ is a selection artefact of our latitude/extinction cuts, which deliberately remove the thin-disc mid-plane; the concentration around $R \simeq 5\text{--}8\,\text{kpc}$ reflects the volume accessible to bright RGB stars interior to the Solar circle and coincides with the molecular ring region where the stellar surface density peaks. *Right*: Metallicity distribution of our data sample. Line colours are the same as in the left panel. 10
- 2 Column-normalised density in the v_ϕ –[M/H] plane. *Left*: the bright-RGB catalogue of [Andrae et al. \[2023\]](#). *Right*: the same sample after all distance, dust, and quality cuts. Greyscale pixels show the normalised counts in each metallicity bin; the red dashed curve is the median v_ϕ , and the black curves trace the 16th and 84th percentiles. 11
- 3 Galactocentric velocity distributions as a function of metallicity. Each panel shows the column-normalised density of stars in the v_R – v_ϕ plane for the metallicity interval printed at the top. With increasing metallicity the distribution contracts in both directions—signalling lower velocity dispersion—while the bulk of stars moves upward to larger prograde azimuthal velocity. 11
- 4 Ellipses mark the approximate extent of the thin disc (black), thick disc (grey), Gaia–Sausage/Enceladus debris (pink) and the pressure-supported stellar halo (purple). The figure serves as a visual key for interpreting the data panels in Fig. 3. 12
- 5 BIC distributions as a function of the number of GMM components in each metallicity bin. The optimum number of components is indicated by the minimum BIC value (highlighted in red). 13
- 6 Gaussian Mixture Model decompositions of the stellar velocity distribution in the v_R – v_ϕ plane for each metallicity bin. The bottom panel of each subfigure shows the 2D velocity distribution with GMM components overplotted as ellipses representing the 1σ contours in v_R – v_ϕ . The top panel shows the fractional contribution. 14
- 7 Ratio of mean rotational velocity to azimuthal velocity dispersion, $V_{\text{rot}}/\sigma_\phi$, for individual GMM components in each metallicity bin. Larger squares correspond to more dominant components. Colours match the GMM components in Figure 6. 17
- 8 Top: Normalized residual maps between observed and GMM-predicted velocity distributions in (v_R, v_ϕ) for the VMP (left) and IMP (right) metallicity bins. Grey ellipses show the 2σ contour of the fiducial thick disc model. Bottom: Disc residuals as a function of injected disc fraction. The dashed line and blue band indicate the observed residual and its uncertainty. The solid black line and red region show mock test results and their uncertainties. 18

9	Density of stars in the $[\alpha/\text{M}]-[\text{M}/\text{H}]$ plane. The high- α and low- α sequences are separated by the piece-wise linear boundary . The transition zone between the two sequences is clearly removed from this plot and discarded from subsequent analysis.	20
10	Mean $[\text{M}/\text{H}]$ colour-coded in the Galactocentric $R-z$ plane. <i>Top</i> : the complete $G < 16$ RGB sample. <i>Bottom left</i> : high- α stars; <i>bottom right</i> : low- α stars. The high- α population is more centrally concentrated and shows a shallower vertical metallicity gradient.	21
11	Azimuthal velocity as a function of metallicity. Each panel shows the column-normalised density in the $[\text{M}/\text{H}]-v_\phi$ plane together with running medians (red dashed) and 16th/84th percentiles (black). Left: full RGB sample. Centre / right: chemically separated high- α and low- α subsamples defined in Sect. 2.	22
12	Distribution of stars in v_R-v_ϕ space across eight metallicity bins (increasing left to right, top to bottom) for the high- α population (top) and low- α population (bottom). The low- α stars are clearly more rotation-supported at high metallicities, while the high- α sample shows a broader velocity structure across all bins, consistent with thick-disc and halo populations.	23
13	BIC scores for different metallicity bins, grouped by high- and low- α populations.	24
14	XD-GMM decomposition of high- α giants in four metallicity bins. Grey ellipses mark the 1σ contours of each Gaussian component.	25
15	XD-GMM decomposition of low- α giants in four metallicity bins. Grey ellipses show the 1σ contours of every Gaussian component.	26

List of Tables

1	Parameters of the Gaussian mixture model fittings in different metallicity bins. The unit for all velocity columns is km s^{-1}	15
2	Number of Gaussian Mixture components selected by the BIC for each metallicity bin, split by α -sequence.	24
3	GMM component weights and kinematics for the high- α sequence. Velocities are in km s^{-1} . Weights indicate the fraction of stars per metallicity bin.	25
4	XD-GMM component weights and kinematics for the low- α sequence. Velocities are in km s^{-1} . Weights are the fractional contribution of each component.	26

1 Introduction

The Milky Way Galaxy, host to our solar system, is a spiral galaxy with a centre located approximately 150 000 trillion miles (or 25 000 lightyears) from Earth. Its formation history is complex and remains an active area of research. Being embedded within the Milky Way means we can study it in greater detail than any external galaxy, testing models of galaxy formation with high-precision observational data. One of the central aims of Galactic Archaeology is to reconstruct the Milky Way’s assembly by examining the chemical compositions and dynamical properties of its stars.

In this project, we replicate and extend the analysis of [Zhang et al. \[2024\]](#), who investigated a very metal-poor disc component in the Milky Way. Very metal poor stars, formed from an interstellar medium unpolluted by earlier generations of supernovae, are among the oldest relics in the Galaxy. Discovering them on disc-like orbits would challenge the conventional view that the disc formed later from already enriched gas [[Bland-Hawthorn and Gerhard, 2016](#)], implying instead an earlier onset of disc assembly. Using Gaia DR3, the original study applied a Gaussian Mixture Model with Extreme Deconvolution to the velocity distributions of stars across metallicity bins, probing whether a coherent disc signal persists down to the lowest metallicities.

1.1 Components of the Milky Way

The Milky Way is commonly decomposed into four stellar components: a *thin disc*, a *thick disc*, a central *bulge/bar*, and a roughly spherical *halo* [[Bland-Hawthorn and Gerhard, 2016](#), [Helmi, 2020](#)]. The thin disc dominates the majority of all stars and most of the interstellar gas in the galaxy. Ongoing star formation is concentrated in the “molecular-gas ring” at Galactocentric radii $R \simeq 4\text{--}8$ kpc, where young ($\lesssim 1$ Gyr), metal-rich stars trace nearly circular, co-rotating orbits with low velocity dispersion ($\sigma_\phi \simeq 20 \text{ km s}^{-1}$). Above the mid-plane lies the thick disc: an older ($\gtrsim 8\text{--}10$ Gyr), moderately metal-poor population with $[\text{Fe}/\text{H}] \sim -0.6$ to -1.0 , a scale height of $z_{\text{scale}} \approx 1$ kpc, and hotter kinematics ($\sigma_z \simeq 40 \text{ km s}^{-1}$) while still retaining net prograde rotation. Inside $R \lesssim 2$ kpc, the central bulge—partly bar-shaped—hosts both old, metal-rich stars and a younger, actively forming component; stellar motions there combine bar-driven streaming with high random velocities ($\sigma \sim 100 \text{ km s}^{-1}$). Encasing all of these is the stellar halo, which contributes only a few per cent of the total stellar mass yet harbours the Galaxy’s oldest, most metal-poor stars ($[\text{Fe}/\text{H}] \lesssim -1.5$) on highly eccentric or even retrograde orbits. Its low density, rich substructure, and extreme kinematics reveal an origin in the hierarchical accretion and tidal disruption of dwarf galaxies and globular clusters. Together, the spatial distribution, chemistry, and dynamics of these four components encode the Milky Way’s star-formation history and its sequence of merger events.

1.2 Metallicity as a Cosmic Clock

Precise ages for individual old stars are notoriously difficult to measure, so their chemical composition - most commonly the iron-to-hydrogen ratio, $[\text{Fe}/\text{H}]$ - is often used as a surrogate clock. Very metal-poor (VMP) stars must have formed before successive generations of Type II and Type Ia supernovae had substantially enriched the interstellar medium, and therefore exhibit low $[\text{Fe}/\text{H}]$ values. Metallicity is inferred spectroscopically from the equivalent widths of metal absorption lines such as Fe I and the Ca II K line; after

correcting for effective temperature and surface gravity, their relative strengths give elemental abundances. Large surveys (for example APOGEE, GALAH, LAMOST, and the Gaia XP spectra) now provide such measurements for millions of stars, enabling empirical age–metallicity relations that link chemistry to stellar chronometry [e.g. Nordström et al., 2004, Haywood et al., 2013, Leung and Bovy, 2019, Anders et al., 2023]. These studies consistently show that stars with $[\text{Fe}/\text{H}] \lesssim -1$ are typically older than ~ 10 Gyr, making low-metallicity populations valuable probes of the Milky Way’s earliest disc-building epochs.

1.3 Λ CDM: hierarchical growth and a lopsided halo

In the concordance Λ CDM model, galaxy-sized haloes assemble hierarchically: small dark-matter clumps form first and then merge to build larger structures. Cosmological N -body simulations demonstrate that the number of subhaloes of mass M obeys $dN/dM \propto M^{-1.9}$, a near power-law over many decades in mass [Cooper et al., 2010, Fall and Chandar, 2012]. For a Milky-Way-sized halo this translates to

- $\sim 10^2$ **minor** accretions with $M_{\text{sub}} \lesssim 10^9 M_\odot$, and
- a few **major** events with $M_{\text{sub}} \gtrsim 10^{10} M_\odot$

over a Hubble time.

Only a small subset of these haloes ever form appreciable numbers of stars. Below a critical virial mass $M_{\text{vir}} \sim 10^{11} M_\odot$, re-ionisation and stellar feedback drastically reduce the efficiency of turning gas into stars. Consequently, the stellar-mass–halo-mass (SMHM) relation becomes very steep at the low-mass end [Purcell et al., 2007, Bullock and Boylan-Kolchin, 2017]: most low-mass subhaloes are effectively “dark”, whereas a few relatively massive dwarfs are luminous.

Hence, while the Milky Way has absorbed hundreds of subhaloes, **one or two** of the most massive dwarfs contribute the majority of the halo’s stellar mass; the rest add little more than dark matter and dynamical substructure.

Once accreted, dynamical friction drags the most massive satellites deep into the Galactic potential, their orbits radialise, and their debris is dispersed throughout the inner halo. The disrupted stars inherit coherent signatures—high radial anisotropy, distinctive angular momenta, and chemically narrow sequences—that survive to the present [e.g. Helmi and Tim de Zeeuw, 2000]. Consequently, the stellar halo is not a smooth spheroid but a map of the Galaxy’s merger history, with the inner halo overwhelmingly shaped by a few dominant progenitors (e.g. Gaia–Sausage/Enceladus), and the outer halo supplied by many low-mass accretions.

1.4 Accretion versus *in-situ* disc formation

Chemical and kinematic evidence confirms that the metal-poor halo is primarily accreted. The debris of the Gaia–Sausage/Enceladus (GSE) event, for instance, is traced by stars with $-2 < [\text{Fe}/\text{H}] < -1$ and extreme orbital anisotropy ($\beta \gtrsim 0.8$; Belokurov et al. 2018, Helmi et al. 2018). At $[\text{Fe}/\text{H}] \lesssim -2$ an even broader mix of minor mergers emerges, erasing any global rotation signal [Lancaster et al., 2019, Bird et al., 2021].

Against this backdrop, a number of studies have uncovered stars in the range $-2 < [\text{Fe}/\text{H}] < -1$ whose velocities resemble a disc: modest eccentricities and net prograde rotation [Norris et al., 1985, Chiba and Beers, 2000, Carollo et al., 2019, An and Beers, 2020]. Gaia has pushed this frontier to $[\text{Fe}/\text{H}] < -2$ [Sestito et al., 2019, Venn et al., 2020, Cordini et al., 2020, Mardini et al., 2022]. Whether these objects represent (i) an *in-situ* metal-poor disc or (ii) the spun-up debris of earlier mergers remains hotly debated.

1.5 Origins of very-metal-poor disc candidates

Three broad formation scenarios have been proposed:

1. **Early *in-situ* disc.** Stars form in a gas-rich disc before $z \sim 4$, and later migrate outward or are dynamically heated; such stars would share the chemistry of the proto-Galaxy.
2. **Proto-galactic building blocks.** VMP stars originate in several massive, gas-rich satellites accreted at high redshift; their debris is dragged into the disc plane as the gaseous disc settles [e.g. Sestito et al., 2020].
3. **Late, minor prograde mergers.** Low-mass satellites on aligned orbits are assimilated after the disc forms, depositing a thin layer of metal-poor stars that retain disc-like kinematics [Santistevan et al., 2021].

Cosmological simulations generally reproduce scenario 2, finding that early mergers dominate the VMP budget while a coherent disc does not appear until $z \lesssim 2$ [Gurvich et al., 2023].

Observationally, Belokurov and Kravtsov [2022] identified *Aurora*, a kinematically hot, weakly rotating population with $-2 \lesssim [\text{Fe}/\text{H}] \lesssim -1.3$, arguing against an extremely early disc. Follow-up work shows Aurora to be centrally concentrated [Rix et al., 2022, Arentsen et al., 2020a,b], consistent with heated debris rather than a long-lived thin disc. Furthermore, secular processes such as bar–halo resonances can impart a modest prograde bias to halo stars, mimicking a disc signal [Dillamore et al., 2023].

Unravelling these possibilities demands six-dimensional phase-space information and precision abundances—the focus of the present study.

1.6 This Work

In this study we assess the claim that the Milky Way hosts a very-metal-poor (VMP; $[\text{Fe}/\text{H}] < -2$) stellar disc. Our data set is drawn from *Gaia* DR3, which supplies six-dimensional phase-space coordinates—sky position, parallax-based distance, proper motions, and radial velocity—for each star, together with homogeneous metallicity and α -element abundances from the *Gaia* XP pipeline. To disentangle kinematic sub-populations we model, in successive narrow metallicity bins, the full three-dimensional velocity distribution (v_R, v_ϕ, v_z) with a Gaussian Mixture Model whose parameters are inferred via *Extreme Deconvolution*; the XD formalism explicitly folds the individual distance and proper-motion uncertainties into the likelihood, ensuring that measurement noise does not bias the recovered velocity moments.

Astrophysically, a genuine disc should manifest itself as a high-weight Gaussian centred near the Local Standard of Rest ($v_\phi \simeq 220 \text{ km s}^{-1}$) with small tangential and vertical

dispersions ($\sigma_\phi, \sigma_z \lesssim 30 \text{ km s}^{-1}$) and negligible mean radial motion, whereas the halo or any heated component should appear as a broad, almost isotropic Gaussian with little net rotation and dispersions of order $120\text{--}150 \text{ km s}^{-1}$. By tracking how the weight of the cold, rotating component varies with metallicity we can determine when ordered rotation first emerged and test whether VMP stars were formed in situ or accreted from a satellite.

2 Data

2.1 Sample construction

Our parent catalogue is the bright ($G < 16$) red-giant-branch sample of [Andrae et al. \[2023\]](#). Stellar metallicities are predicted with an eXtreme-Gradient-Boosting model trained on high-resolution APOGEE DR17 spectra and a supplementary set of very metal-poor stars, ensuring reliable performance down to $[\text{M}/\text{H}] \simeq -3.5$. For each of the 17.6 million giants the catalogue delivers homogeneous values of $[\text{M}/\text{H}]$, T_{eff} , and $\log g$ with a quoted random uncertainty of $\simeq 0.1 \text{ dex}$ in $[\text{M}/\text{H}]$ at $G \lesssim 15$. The catalogue only retains entries flagged as “high-confidence” and lying in $-3.5 < [\text{M}/\text{H}] < +0.5$.

Astrometric positions, proper motions, and radial velocities come from the main *Gaia* DR3 tables [[Gaia Collaboration et al., 2023](#)], while heliocentric distances are adopted from the Bayesian photo-geometric catalogue of [Bailer-Jones et al. \[2021\]](#). Because accurate velocities scale with distance precision, we impose a fractional-parallax-uncertainty cut $\sigma_\varpi/\varpi < 0.10$ (FPU); stars that fail this threshold are discarded.

XP spectra are susceptible to reddening: heavy extinction dims the sources, lowers the XP signal-to-noise ratio, and biases the machine-learning metallicities. To minimise such systematics we exclude stars with $E(B-V)_{\text{SFD}} > 0.5$ or Galactic latitude $|b| < 10^\circ$, using colour-excess values from the SFD map accessed via DUSTMAPS [[Green, 2018](#)]. These criteria remove regions where dust corrections are large and spatially variable, at the expense of a modest loss of sky coverage.

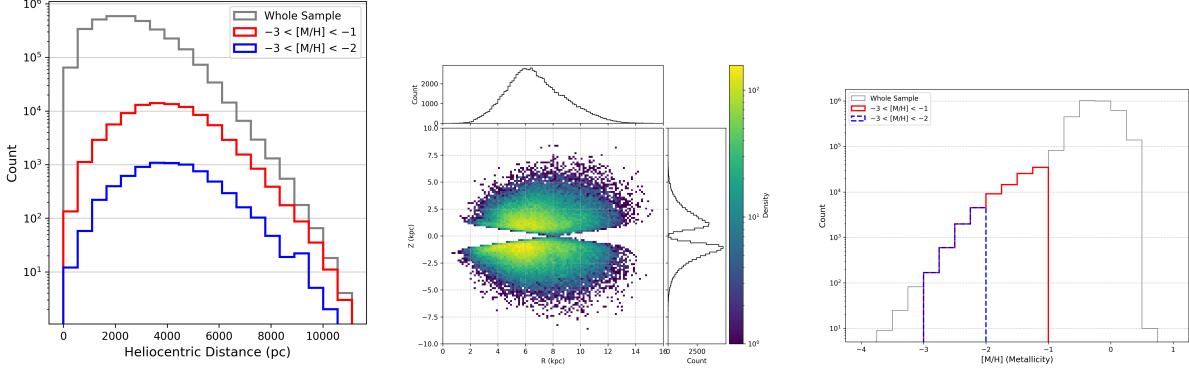
Field-star kinematics can also be skewed by dense sub-structures. Accordingly we mask all objects lying within 1° of any known globular cluster or dwarf-galaxy satellite, following the list compiled by [Pace \[2024\]](#). This step eliminates obvious non-field populations (e.g. cluster members and recent accretion debris) without significantly reducing the statistical power of the sample.

After the metallicity flag, distance-quality, reddening, latitude, and sub-structure cuts, our working data set comprises $\sim 3.4 \times 10^6$ red-giant stars possessing homogeneous metallicities and full six-dimensional phase-space information. This curated sample underpins the chemo-kinematic analysis presented in the remainder of this report.

2.2 Galactocentric Positions and Velocities

Six-dimensional phase-space coordinates are obtained with `astropy.coordinates`. We adopt a Galactocentric frame with $R_0 = 8.1 \text{ kpc}$ and $Z_0 = 25 \text{ pc}$ [[McMillan, 2016](#)], and a solar velocity¹ $(U_\odot, V_\odot, W_\odot) = (11.1, 245, 7.25) \text{ km s}^{-1}$ [[Schönrich et al., 2010](#)]. The

¹Cartesian components (U, V, W) , where U is radially outwards, V is aligned with Galactic rotation, and W points to the North Galactic Pole.



(a) Heliocentric distance

(b) R - Z distribution

(c) Metallicity

Figure 1: Properties of the final RGB sample after all quality and footprint cuts. *Left:* heliocentric-distance histogram for the whole sample (grey); the subsets with $-3 < [\text{M}/\text{H}] < -1$ and $-3 < [\text{M}/\text{H}] < -2$ are shown in solid red and dashed blue, respectively. *Middle:* density map in Galactocentric cylindrical coordinates. The empty band at low $|Z|$ is a selection artefact of our latitude/extinction cuts, which deliberately remove the thin-disc mid-plane; the concentration around $R \simeq 5\text{--}8\text{ kpc}$ reflects the volume accessible to bright RGB stars interior to the Solar circle and coincides with the molecular ring region where the stellar surface density peaks. *Right:* Metallicity distribution of our data sample. Line colours are the same as in the left panel.

cylindrical velocity components (v_R, v_ϕ, v_Z) are extracted from the transformed SkyCoord module.

To propagate measurement errors we generate $N_{\text{MC}} = 100$ Monte-Carlo realisations per star, drawing parallax, proper motions, radial velocity, and distance from their reported uncertainties (the proper-motion covariance is honoured through a bivariate normal). Each realisation is transformed to the Galactocentric frame, yielding distributions of v_R , v_ϕ , and v_Z ; the 1σ widths of those distributions are stored as per-star velocity uncertainties.

As shown in Figure 2, stellar azimuthal velocities evolve increase with metallicity. Halo-like kinematics dominate at $[\text{M}/\text{H}] \lesssim -1.5$ with statistics indicative of a pressure-supported component. A rapid spin-up appears over the metallicity range $[\text{M}/\text{H}] \simeq -1.3$ to -0.9 , consistent with Belokurov and Kravtsov [2022]. By $[\text{M}/\text{H}] \gtrsim -0.5$ the stellar azimuthal velocities reaches the Local Standard-of-Rest value ($\approx 220 \text{ km s}^{-1}$) and the velocity dispersion dispersion falls, marking the transition to a disc. Visually, using 2, we can observe that the onset of ordered rotation in the Milky Way occurred when the inter-stellar medium reached roughly one-tenth solar metallicity.

As shown in Fig. 3, stars with $[\text{M}/\text{H}] \geq -1.0$ have a strong prograde bias in azimuthal velocities, with a peak at $v_\phi \gtrsim 180 \text{ km s}^{-1}$ and a relatively narrow distribution in v_R . As shown in Fig. 4, this is consistent with the thin- and thick-disc ellipses. Below $[\text{M}/\text{H}] \simeq -1.0$ the distribution broadens and drops toward $v_\phi \approx 0$, indicating pressure supported kinematics, characteristic of the stellar halo and the radial Gaia-Sausage/Enceladus debris. At the lowest metallicities ($[\text{M}/\text{H}] \lesssim -1.5$) the contours are nearly isotropic with only a mild prograde bias. Hence, any rotation-supported very-metal-poor disc must contribute at most a small fraction of the population. In subsequent analysis we quanti-

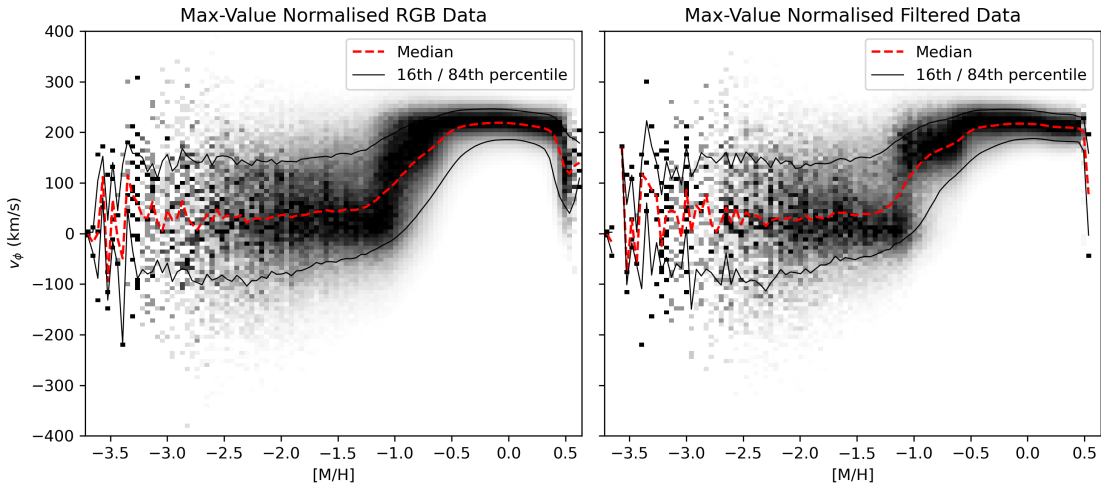


Figure 2: Column-normalised density in the v_ϕ -[M/H] plane. *Left:* the bright-RGB catalogue of Andrae et al. [2023]. *Right:* the same sample after all distance, dust, and quality cuts. Greyscale pixels show the normalised counts in each metallicity bin; the red dashed curve is the median v_ϕ , and the black curves trace the 16th and 84th percentiles.

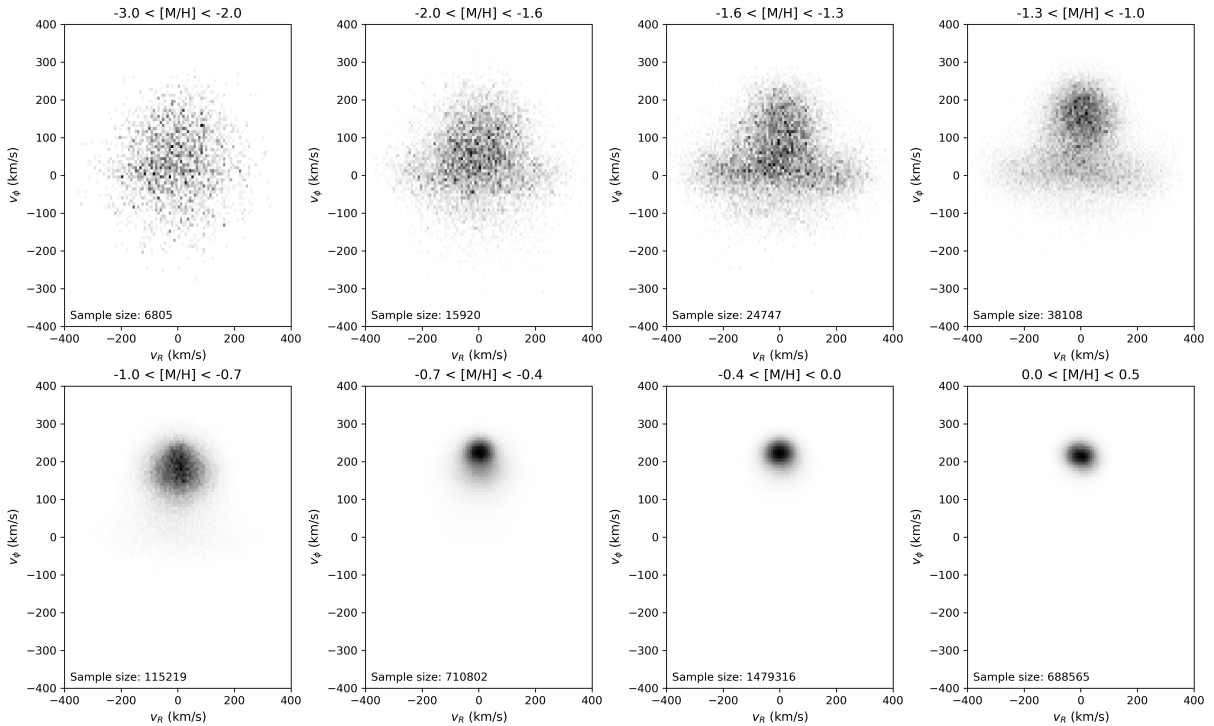


Figure 3: Galactocentric velocity distributions as a function of metallicity. Each panel shows the column-normalised density of stars in the v_R - v_ϕ plane for the metallicity interval printed at the top. With increasing metallicity the distribution contracts in both directions—signalling lower velocity dispersion—while the bulk of stars moves upward to larger prograde azimuthal velocity.



Figure 4: Ellipses mark the approximate extent of the thin disc (black), thick disc (grey), Gaia–Sausage/Enceladus debris (pink) and the pressure-supported stellar halo (purple). The figure serves as a visual key for interpreting the data panels in Fig. 3.

tatively assess these observations.

Given we are testing whether a very-metal-poor stellar disc exists, we naturally restrict the sample to stars within $|Z| < 2.5$ kpc of the galactic mid-plane. This keeps the focus on stars close to the plane, where any disc-like population (whether formed in situ or deposited by mergers) would be found [Tkachenko et al., 2025].

Upon comparison with Zhang et al. [2024], we note that our sample is approximately the same size - with a difference of less than 0.002% of the sample size in each bin.

3 Methodology

3.1 Gaussian Mixture Model

To quantitatively investigate the kinematic structure of metal-poor stars and assess the presence of a potential very-metal-poor disc, we use a Gaussian Mixture Model (GMM) framework as done by Zhang et al. [2024]. GMMs are a class of unsupervised machine learning algorithms commonly used in data science for clustering and density estimation. They model a dataset as a weighted sum of multivariate Gaussian distributions, each corresponding to a latent sub-population within the data.

From a probabilistic perspective, the GMM assumes that each observed data point is generated from a hidden (latent) variable indicating membership in one of the Gaussian components. This latent space formulation allows the model to assign probabilistic classifications to data points, providing a soft clustering where each star has a fractional likelihood of belonging to each component. In our case, the data are three-dimensional velocity vectors (v_R, v_ϕ, v_Z) , and the latent space captures distinct kinematic substructures in this space.

We implement the GMM fitting using the pyGMMis package [Melchior and Goulding, 2016] in the v_R , v_ϕ , and v_Z phase space. This algorithm extends the standard Expectation-Maximisation (EM) algorithm with the “Extreme Deconvolution” technique developed by Bovy et al. [2011]. This method is particularly well-suited to astronomical datasets, as it incorporates measurement uncertainties into the GMM fitting by modifying the EM

updates to account for known errors on each data point. In our case, these uncertainties are derived from the Gaia astrometric and spectroscopic data and are represented by diagonal covariance matrices encoding the squared uncertainties in v_R , v_ϕ , and v_Z for each star.

3.2 Number of Gaussian Components

We apply the GMM separately to each metallicity bin with $[M/H] < -1$, as we are specifically interested in detecting any rotationally supported structure among the very metal-poor stars. An important decision must be made when implementing the appropriate number of components in applying Gaussian Mixture Models. Too few components may underfit the data, missing real substructures, while too many will overfit, leading to spurious and physically uninterpretable results.

We select the optimal number of components using the Bayesian Information Criterion (BIC) [Schwarz 1978](#). The BIC is defined as

$$BIC = k \ln(n) - 2 \ln \mathcal{L}, \quad (1)$$

where $k = (1 + 3 + 6) \times N - 1$ is the total number of free parameters in a model with N Gaussian components (accounting for the weights, means, and covariances), n is the number of stars in the sample, and \mathcal{L} is the maximum likelihood of the fit. The BIC penalizes model complexity, such that adding extra components without a significant gain in likelihood will result in a higher BIC value.

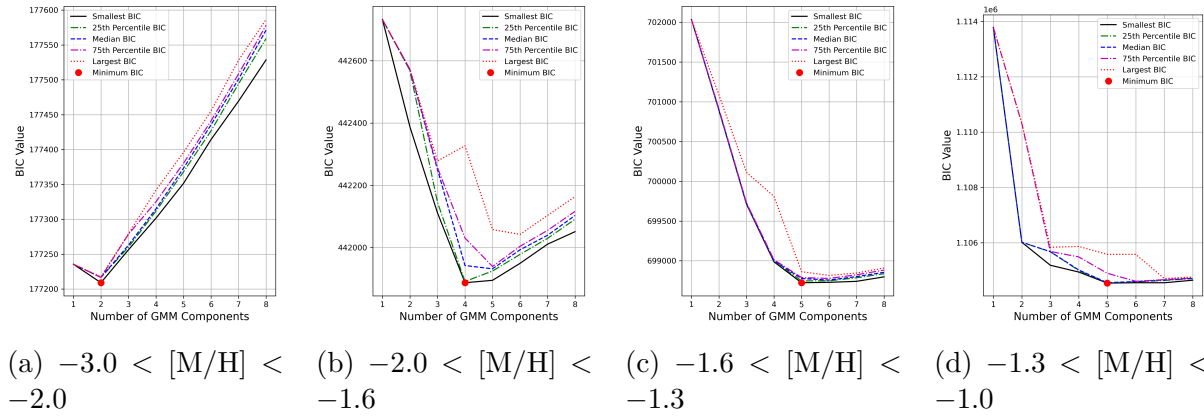


Figure 5: BIC distributions as a function of the number of GMM components in each metallicity bin. The optimum number of components is indicated by the minimum BIC value (highlighted in red).

The Expectation-Maximisation algorithm can become trapped in local minima, so we performed 50 initialisations for each N and recorded the BIC value for each trial. The minimum BIC value across all trials indicated the statistically preferred model and suggests that the global optimum was likely reached.

To improve convergence and model stability, the GMM components in each trial were initialised using the kmeans algorithm. This is due to the sensitivity of GMMs to their starting conditions: poor initialisation can lead to convergence on undesirable solutions, particularly in high-dimensional or overlapping data. KMeans clustering provides

an initialisation point by partitioning the velocity space into compact, roughly spherical clusters. This works well with the assumptions of Gaussian components and often gives faster, more stable convergence and more physically meaningful results. In our application, where stellar substructures are partially overlapping in velocity space, this method applies well.

In Figure 5, we show the distribution of BIC values across four metallicity bins as a function of N . The resulting preferred number of components are 2, 4, 5, and 5 for the VMP, IMP, MP1, and MP2 bins. This is in agreement with the findings of [Zhang et al. \[2024\]](#). Our analysis, however, selects the lowest BIC each time, removing the need for a subjective choice of the number of components when BIC values are very similar. [Zhang et al. \[2024\]](#), when observing the BIC values for the MP1 bin chooses to use 5 components instead of 6 despite the BIC score for the 6-component model being lower than the 5-component model.

4 Results

4.1 Gaussian Mixture Model Fit

Using the number of components selected by the BIC criteria, we fit the GMM to the data in each metallicity bin as shown in Figure 6. We increased the number of initialisations to 100 for the final fitting to ensure convergence to a stable solution.

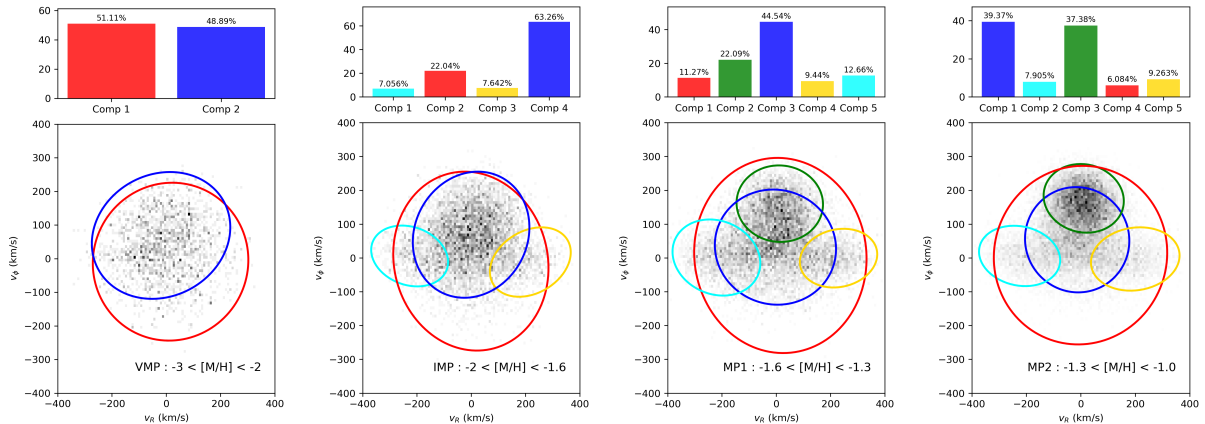


Figure 6: Gaussian Mixture Model decompositions of the stellar velocity distribution in the v_R - v_ϕ plane for each metallicity bin. The bottom panel of each subfigure shows the 2D velocity distribution with GMM components overplotted as ellipses representing the 1σ contours in v_R - v_ϕ . The top panel shows the fractional contribution.

As shown in Figure 6, the GMM is able to capture kinematic substructures in the velocity space of metal-poor stars. As metallicity increases, a gaussian component with a clear prograde rotation signal emerges (in green), indicative of a disc-like structure. The statistics of the GMM fit are summarised in Table 1, which lists the weights, means, and dispersions of each component in the four metallicity bins.

At $[M/H] < -1.6$ (the VMP and IMP regimes), a disc component is not observed. Instead, the kinematic structure is dominated by a prograde halo and a stationary halo. In the VMP bin, the sample is almost evenly split between these two components, with

Components	Weights (%)	v_R	σ_R	v_ϕ	σ_ϕ	v_Z	σ_Z
VMP: $-3.0 < [\text{M}/\text{H}] < -2.0$ (4768 stars)							
Stationary halo	51.1	15.86	143.17	-9.13	117.36	-0.08	122.64
Prograde halo	48.9	-19.14	127.43	68.86	94.28	-0.90	82.89
IMP: $-2.0 < [\text{M}/\text{H}] < -1.6$ (12052 stars)							
Stationary halo	22.0	-1.45	142.88	-9.59	132.32	-0.91	124.92
Prograde halo	63.3	-0.58	107.32	68.52	93.27	-1.16	72.56
GS/E(1)	7.1	-226.92	70.78	5.60	44.98	8.43	88.40
GS/E(2)	7.6	217.52	74.41	-12.35	51.35	-4.22	89.78
MP1: $-1.6 < [\text{M}/\text{H}] < -1.3$ (19142 stars)							
Stationary halo	11.3	15.09	158.68	7.11	144.33	-2.55	132.08
Prograde halo	44.5	-3.02	111.54	31.79	85.15	-0.54	70.36
GS/E(1)	12.7	-220.40	80.76	1.01	56.29	0.47	91.00
GS/E(2)	9.4	229.32	71.22	-0.82	43.42	1.42	92.69
Thick disc	22.1	12.93	79.56	160.32	56.58	-2.31	68.83
MP2: $-1.3 < [\text{M}/\text{H}] < -1.0$ (30892 stars)							
Stationary halo	6.1	-1.17	159.06	8.07	132.05	-3.37	120.46
Prograde halo	39.4	-13.47	95.65	53.64	77.86	-3.04	71.00
GS/E(1)	7.9	-224.68	74.44	5.73	44.63	2.41	87.27
GS/E(2)	9.3	199.71	81.28	-3.30	46.84	-2.07	88.99
Thick disc	37.4	10.56	73.55	176.07	50.79	0.85	62.03

Table 1: Parameters of the Gaussian mixture model fittings in different metallicity bins. The unit for all velocity columns is km s^{-1} .

the stationary halo contributing 51.1% and the prograde halo 48.9%. Both show broad velocity dispersions, with only modest rotational support ($\langle v_\phi \rangle \sim 69 \text{ km s}^{-1}$ for the prograde halo) and no evidence for a kinematically cold disc-like structure.

In the IMP bin, the picture remains qualitatively similar, although the prograde halo dominates more strongly (63.3%) and additional substructure becomes apparent. Two minor components, interpreted as fragments of the Gaia–Sausage/Enceladus (GS/E) merger debris, are also identified, each contributing $\sim 7\%$ of the population and exhibiting highly radial orbits ($|v_R| > 200 \text{ km s}^{-1}$). These GS/E components are characterised by strong anisotropy and contribute to the broadening of the halo distribution, but again show no signature of disc-like kinematics. The absence of a cold, rotating disc in these bins suggests that if a very-metal-poor disc exists, it must be a minor contributor to the local stellar population.

Our GMM decomposition recovers the same substructures identified by [Zhang et al. \[2024\]](#) across all metallicity bins. We find similar velocity dispersions and centroid trends for the stationary halo, prograde halo, and GS/E components. Notably, our model assigns a more comparable weight to the prograde halo component in the VMP bin, in contrast to the dominant stationary halo reported by [Zhang et al. \[2024\]](#). We also observe some variation in the centroid v_ϕ values of GS/E substructures, although their bimodal spatial structure is preserved.

4.2 Rotational Support and the Onset of Disc Formation

To assess the degree of rotational support in each component, we compute the ratio $V_{\text{rot}}/\sigma_\phi$, where V_{rot} is the mean azimuthal velocity and σ_ϕ its dispersion. This ratio serves as a conventional diagnostic of disc-like kinematics, with values $\gtrsim 3$ indicating rotation-supported populations. As shown in Figure 7, all components in the VMP and IMP bins fall below this threshold, confirming that the GMM identifies only dynamically hot, dispersion-supported structures in these regimes. This is consistent with the interpretation of the dominant components as stationary and prograde halo populations, with $V_{\text{rot}}/\sigma_\phi \approx 0.7$ in both cases (see also Table 1).

At higher metallicities, a dynamically colder disc population emerges. In the MP1 bin, the thick disc component (green) rotates at $v_\phi \sim 160 \text{ km s}^{-1}$ with $\sigma_\phi \sim 57 \text{ km s}^{-1}$, yielding $V_{\text{rot}}/\sigma_\phi \approx 2.8$. While just below the canonical boundary, this component's low vertical dispersion and substantial weight (22.1%) mark it as a distinct disc-like structure. By the MP2 bin, the disc becomes the dominant component (37.4%), with $V_{\text{rot}}/\sigma_\phi \approx 3.5$, indicating clear rotational support and a well-established thick disc. These trends point to a sharp transition in the stellar kinematics around $[\text{M}/\text{H}] \sim -1.5$, consistent with the early onset of disc formation.

Meanwhile, the GS/E components — identifiable in the IMP, MP1, and MP2 bins — remain dynamically distinct, with high $|v_R|$, relatively small v_ϕ , and negligible rotational support, reinforcing their origin as debris from a major radial merger [Helmi et al., 2018]. Notably, given the estimated time of the GS/E accretion event (of order 8–11 Gyr ago [Gallart et al., 2019, Belokurov et al., 2020, Di Matteo et al., 2019]), its stellar debris is expected to be phase-mixed. This implies that the positive and negative v_R components should contribute approximately equally. This symmetry is indeed observed in the two MP bins. However, in the IMP bin the distribution is clearly asymmetric, with the negative v_R GS/E component (aqua) containing nearly twice as many stars as the positive one (orange). This may suggest incomplete phase mixing or contamination by other structures at this intermediate metallicity.

4.3 Residual Analysis for Hidden Disc Populations

One of the limitations of GMMs is that they can fail to detect substructures that contribute only weakly to the overall distribution. To address this, we perform a residual analysis to test whether a disc-like population—too weak to be picked up by the GMM—might nonetheless be present in the VMP and IMP metallicity regimes.

We generated a synthetic dataset by drawing the same number of mock stars as observed stars from the best-fit GMM in each bin. Since our GMM uses the Extreme Deconvolution algorithm, which accounts for observational uncertainties during fitting, the raw samples from the model are noise-free. However, comparing these directly to real data would be inappropriate due to the absence of measurement error. To resolve this, we assign each mock star the velocity uncertainties of its nearest neighbour in the observed data (in (v_R, v_ϕ, v_Z) space), and then add Gaussian noise according to these uncertainties.

We then bin both the observed and mock data in the (v_R, v_ϕ) plane and compute the normalized residual map, defined as

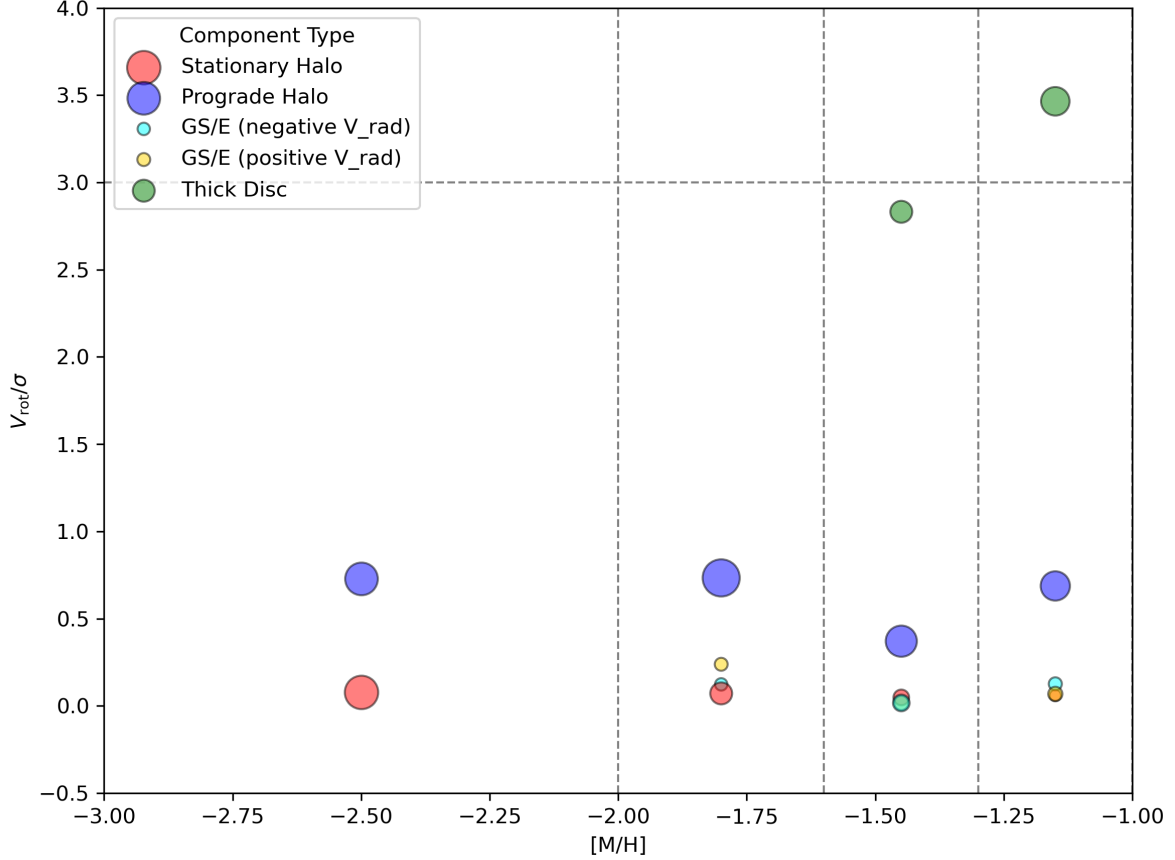


Figure 7: Ratio of mean rotational velocity to azimuthal velocity dispersion, $V_{\text{rot}}/\sigma_\phi$, for individual GMM components in each metallicity bin. Larger squares correspond to more dominant components. Colours match the GMM components in Figure 6.

$$H_{\text{residual}} = \frac{H_{\text{obs}} - H_{\text{mock}}}{H_{\text{obs}} + H_{\text{mock}} + \epsilon},$$

where H_{obs} and H_{mock} are the 2D histograms and $\epsilon = 10^{-5}$ is added to avoid division by zero. The residual maps are shown in the top row of Figure 8 for the VMP and IMP bins. The grey dashed ellipses highlight a 2σ region of a hypothetical thick disc with mean velocity $(v_R, v_\phi) = (0, 180)$ km s $^{-1}$ and dispersions $(\sigma_R, \sigma_\phi) = (70, 50)$ km s $^{-1}$, consistent with the thick disc component seen in the MP2 metallicity bin.

To quantify the possible presence of a hidden disc, we count the excess number of observed stars inside this thick disc ellipse relative to the GMM-generated sample. We repeat this calculation for 200 Monte Carlo realizations to estimate the residual and its uncertainty. The results are shown as horizontal dashed lines in the bottom row of Figure 8, representing a disc-like residual of 40.4 ± 24.8 stars in the VMP bin and 76.9 ± 42.8 stars in the IMP bin.

To interpret these residuals, we repeat the same procedure but now inject a mock disc population—generated from the same thick disc Gaussian—into the GMM baseline. By varying the injected disc fraction from 0% to 5% of the sample and recalculating the residual each time, we construct a relationship between disc fraction and expected

residual. This is shown as the solid black line in the bottom panels of Figure 8, with the red shaded region indicating the 1σ uncertainty across Monte Carlo trials.

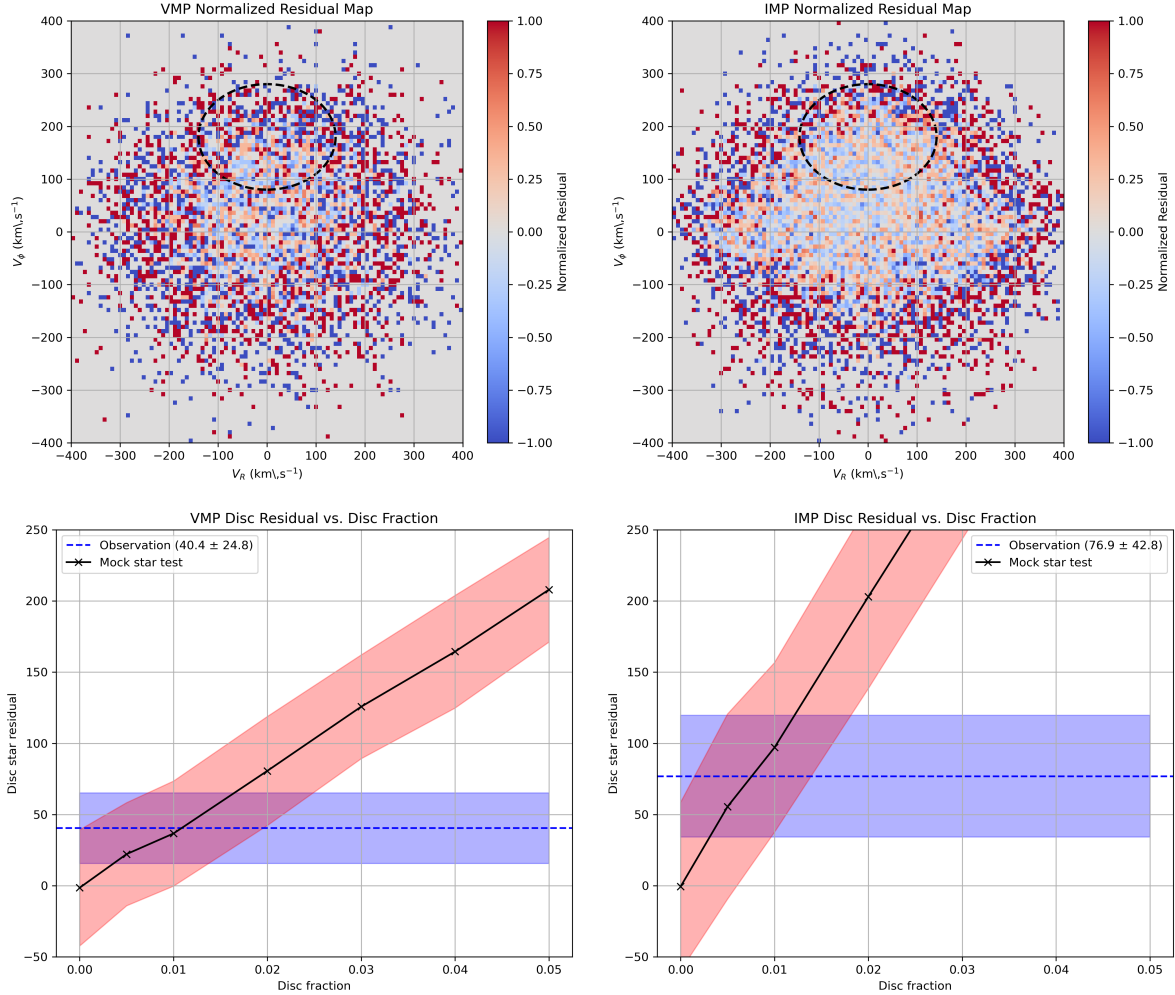


Figure 8: Top: Normalized residual maps between observed and GMM-predicted velocity distributions in (v_R, v_ϕ) for the VMP (left) and IMP (right) metallicity bins. Grey ellipses show the 2σ contour of the fiducial thick disc model. Bottom: Disc residuals as a function of injected disc fraction. The dashed line and blue band indicate the observed residual and its uncertainty. The solid black line and red region show mock test results and their uncertainties.

5 Extension analysis

5.1 Alpha-element abundance

We extend the chemo-kinematic analysis by adding the alpha-to-iron ratio $[\alpha/\text{Fe}]$, where the “alpha” elements (O, Ne, Mg, Si, S, Ca, Ti) are produced almost entirely in core-collapse (Type II) supernovae, whereas most iron is released later by thermonuclear (Type Ia) explosions. Because the two channels operate on very different time-scales— $\sim 10\text{--}30$ Myr for Type II versus $\gtrsim 0.1\text{--}1$ Gyr for Type Ia—the quantity $[\alpha/\text{Fe}]$ encodes the star-formation history of a stellar population:

- **High** $[\alpha/\text{Fe}]$. Rapid, intense star formation finished before large numbers of Type Ia events enriched the gas with iron. This chemistry is typical of the thick disc, the stellar halo and ancient accreted debris.
- **Low** $[\alpha/\text{Fe}]$. A more prolonged formation history allowed Type Ia ejecta to accumulate, diluting the alpha enhancement. The present-day thin disc and metal-rich bulge occupy this regime.

Hence the $[\alpha/\text{Fe}]$ – $[\text{M}/\text{H}]$ plane acts as a chemical clock: populations that overlap in $[\text{M}/\text{H}]$ but differ in formation time-scale separate cleanly in $[\alpha/\text{Fe}]$.

Following Viswanathan et al. [2024], we divide the sample into high- and low- $[\alpha/\text{M}]$ sequences using data from Li et al. [2023] and fit an error-convolved Gaussian-mixture model as done in previous analysis. Before fitting, chemical-evolution arguments already set some expectations. In the *high- α branch* we should see a non-rotating halo Gaussian below $[\text{M}/\text{H}] \approx -1.6$, joined by a prograde, kinematically hot “thick-disc” component that quickly gains weight between $[\text{M}/\text{H}] \simeq -1.6$ and -1.0 and dominates for $[\text{M}/\text{H}] > -0.7$. In the *low- α branch* a halo Gaussian alone is expected below $[\text{M}/\text{H}] \approx -1.3$, while a cold, high-weight thin-disc Gaussian—centred near the local standard of rest with $\sigma \lesssim 30 \text{ km s}^{-1}$ —should emerge after this. However, due to selection effects, the thin disc is expected to not be identified - we are interested in disk formation.

5.2 Data

We obtain the α -to-metal abundance ratios from the XP-based catalogue of Li et al. [2023], whose neural-network model—trained on high-resolution APOGEE DR17 spectra—achieves a typical precision of $\simeq 0.05$ dex for bright sources ($G < 16$). The α catalogue is first cross-matched with the metallicity-selected red-giant branch sample described in Section 2.1. To guarantee photometric and astrometric fidelity we then enforce

- $G < 16$ and a parallax signal-to-noise ratio $\varpi/\sigma_\varpi > 5$;
- an effective-temperature cut $T_{\text{eff}} < 5200 \text{ K}$ to remove hot stars whose XP metallicities are known to be biased low;
- red-giant selections on the Hertzsprung–Russell diagram ($\log g < 3.5$, together with the magnitude-colour cuts² $M_{W1} > -0.3 - 0.006(5500 - T_{\text{eff}})$, $M_{W1} > -0.01(5300 - T_{\text{eff}})$, and $(G - W2) < 0.2 + 0.77(G_{\text{BP}} - W1)$);
- rejection of stars within 1 degree of known dwarf galaxies and in known globular clusters.
- a reddening cut $E(B - V) < 0.5$ to remove stars in the Galactic plane, where the dust extinction is high and the XP metallicities are known to be biased.
- a latitude cut $|b| > 10^\circ$ to remove stars in the Galactic plane, where the dust extinction is high and the XP metallicities are known to be biased.
- in this analysis we do not remove stars with a fractional parallax uncertainty cut as done in Section 2.1. This cut removes a significant fraction of stars in the very-metal-poor regime, which is the focus of this analysis.

² $M_{W1} = W1 + 5 \log_{10}(\varpi/100)$

We obtain approximately 3.4 million stars in our final sample with alpha element abundances.

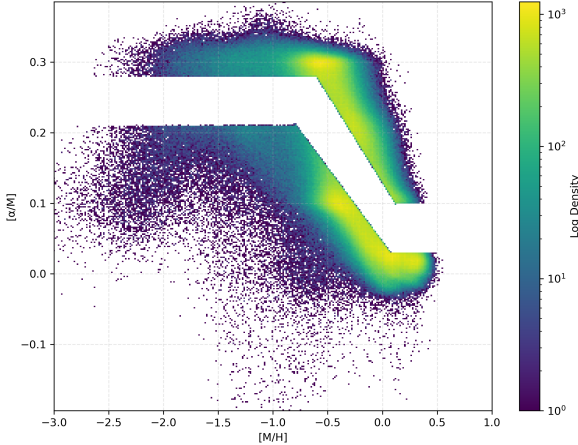


Figure 9: Density of stars in the $[\alpha/M]$ – $[M/H]$ plane. The high- α and low- α sequences are separated by the piece-wise linear boundary . The transition zone between the two sequences is clearly removed from this plot and discarded from subsequent analysis.

Figure 9 displays the logarithmic density of our RGB sample in the $[\alpha/M]$ – $[M/H]$ plane. Following Chandra et al. [2024], but with a deliberately *tighter* boundary, we separate the two sequences with the piece-wise relations

$$\text{high-}\alpha : \begin{cases} [M/H] < -0.60 & [\alpha/M] > 0.28 \\ -0.60 \leq [M/H] \leq 0.125 & [\alpha/M] > -0.25[M/H] + 0.13 \\ [M/H] > 0.125 & [\alpha/M] > 0.10 \end{cases}$$

$$\text{low-}\alpha : \begin{cases} [M/H] < -0.80 & [\alpha/M] < 0.21 \\ -0.80 \leq [M/H] \leq 0.07 & [\alpha/M] < -0.21[M/H] + 0.04 \end{cases}$$

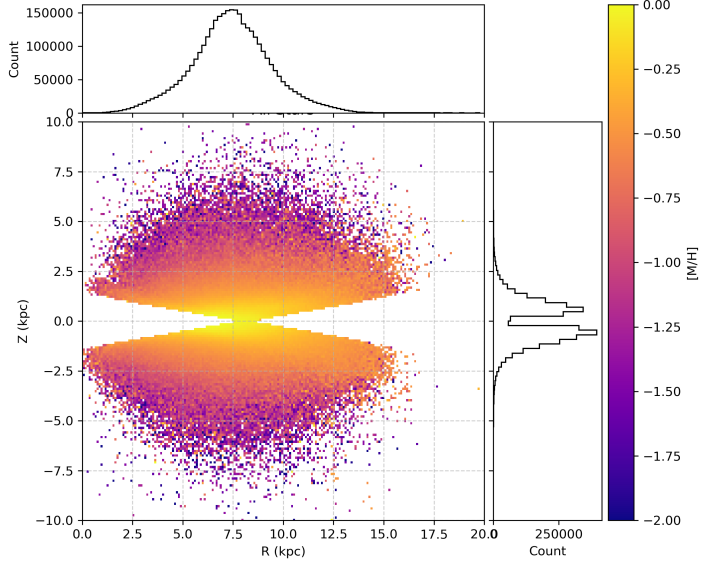
and discard the intermediate “transition” band.

This prescription departs slightly from the cuts adopted by Chandra et al. [2024]: our high- α threshold is raised so that the chemistry of the Gaia–Sausage/Enceladus debris [Belokurov et al., 2018, Helmi et al., 2018] does not leak into the in-situ sequence; and the exclusion band is widened to maximise purity in both sub-samples.

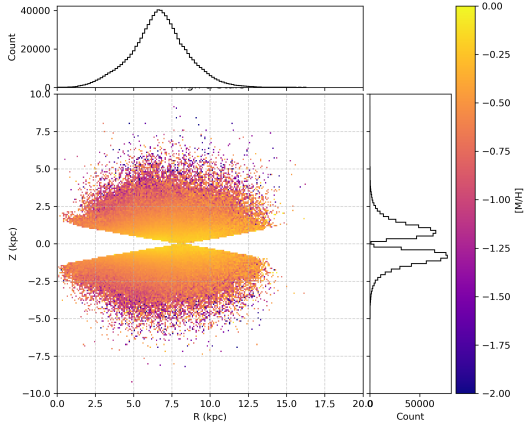
Figure 10 shows how metallicity varies with Galactocentric radius R and height z . The all-star map already hints at a global decline in $[M/H]$ away from the plane and the Solar circle, albeit modulated by the dust-driven selection hole around $z \approx 0$.

The high- α giants occupy a comparatively compact domain, $R \lesssim 10$ kpc and $|z| \lesssim 3$ kpc, and display only a gentle vertical gradient of $\simeq -0.15$ dex kpc $^{-1}$. Such behaviour is expected for the old, kinematically hot thick disc that formed rapidly in the inner Galaxy.

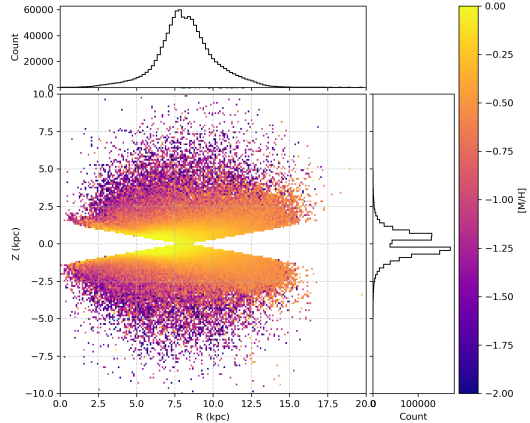
By contrast, low- α stars extend to $R \gtrsim 14$ kpc and $|z| \approx 5$ kpc. Their mean metallicity falls steeply with height (approx. -0.35 dex kpc $^{-1}$) and with radius, producing the flared, metal-poor outskirts typical of the thin disc after radial migration [Haywood et al., 2013]. The larger scale-height range also accommodates halo contaminants, especially at low R .



(a) All RGB stars



(b) High- α subsample



(c) Low- α subsample

Figure 10: Mean $[M/H]$ colour-coded in the Galactocentric $R-z$ plane. *Top*: the complete $G < 16$ RGB sample. *Bottom left*: high- α stars; *bottom right*: low- α stars. The high- α population is more centrally concentrated and shows a shallower vertical metallicity gradient.

Figure 11 shows chemo-kinematic behaviour for the two disc sequences. In the low- α panel the thin disc dominates for $[M/H] \gtrsim -1$: stars cluster around $v_\phi \simeq 200 \text{ km s}^{-1}$ with a small dispersion, while at $[M/H] \lesssim -1$ the distribution flips to a radially biased, low-rotation component characteristic of accreted debris. The transition resembles a step function centred on $[M/H] \simeq -1.0$.

High- α giants show a monotonic spin-up: metal-poor stars ($[M/H] \lesssim -2$) rotate slowly ($v_\phi \approx 50 \text{ km s}^{-1}$) but gain angular momentum steadily, merging into a kinematically colder high- α disc by $[M/H] \simeq -0.7\text{--}0.5$ ($v_\phi \approx 180 \text{ km s}^{-1}$). This continuous trend supports a scenario in which the proto-Galaxy's in-situ population gradually spun up as star formation progressed, while the hotter tail reflects residual halo and early-merger contamination that our α cut cannot entirely remove.



Figure 11: Azimuthal velocity as a function of metallicity. Each panel shows the column-normalised density in the $[M/H]$ – v_ϕ plane together with running medians (red dashed) and 16th/84th percentiles (black). Left: full RGB sample. Centre / right: chemically separated high- α and low- α subsamples defined in Sect. 2.

Following the method described in Section 2.2, we obtain full six-dimensional phase-space coordinates for the chemically separated high- and low- α subsamples. Figure 12 shows the distribution of stars in the v_R – v_ϕ plane across metallicity bins for the high- α (top) and low- α (bottom) populations.

The low- α sample exhibits a strong rotationally supported component, particularly at higher metallicities ($[M/H] \gtrsim -1.0$), with a narrow v_ϕ distribution centred around ~ 200 km/s and low radial velocity dispersion—clear hallmarks of thin-disc kinematics. As metallicity decreases, this rotational component becomes less pronounced, with broader distributions in both v_R and v_ϕ appearing at $[M/H] \lesssim -1.5$, consistent with increased contamination from halo or accreted populations.

The high- α stars, by contrast, show a continuous transition from a kinematically hot, low-rotation regime at low metallicities to a more rotation-supported disc at higher metallicities. This reflects the gradual build-up of the thick disc over time, as also noted in Chandra et al. [2024]. The velocity dispersion is broader throughout, indicating that high- α stars trace older, more dynamically heated populations.

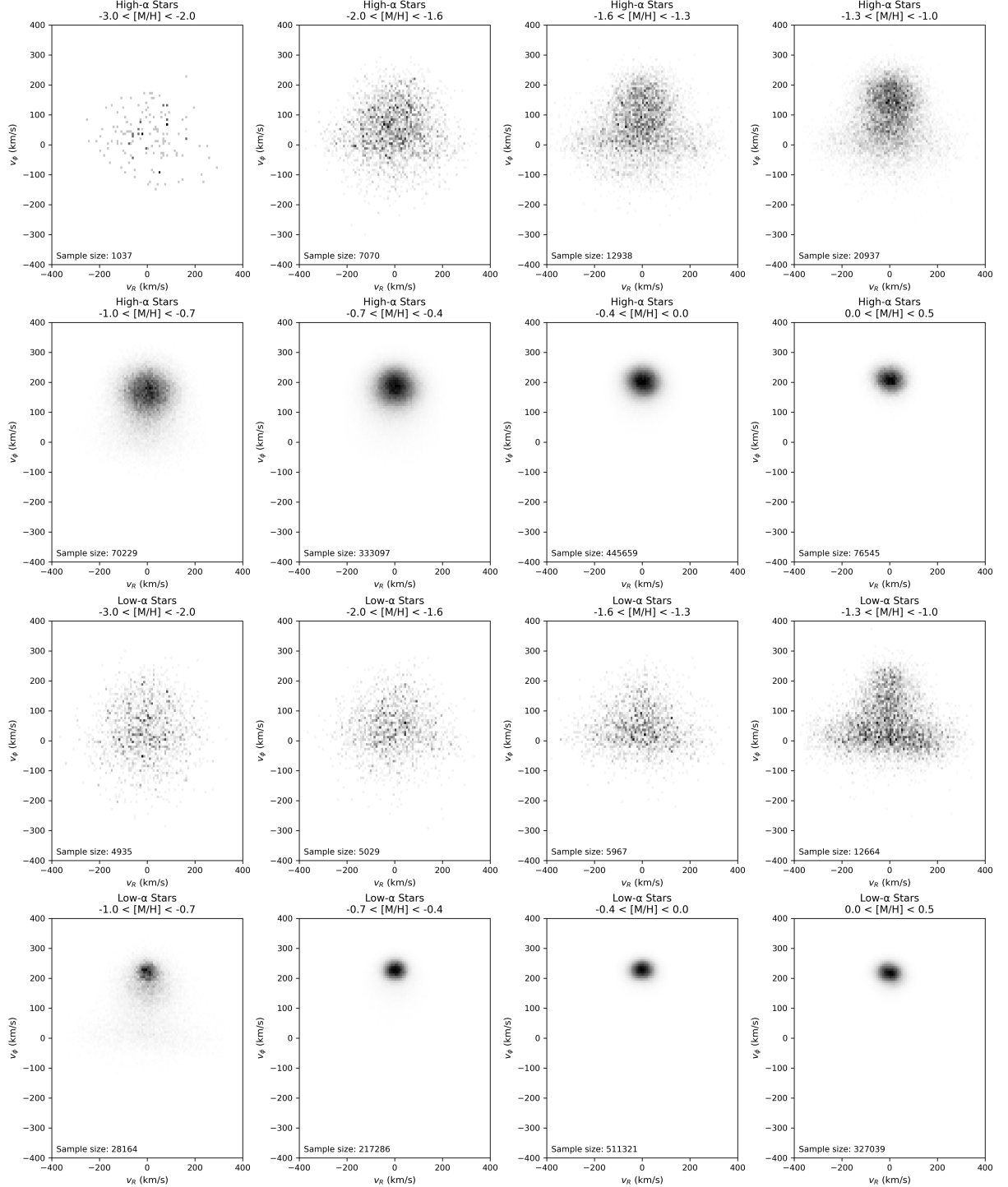


Figure 12: Distribution of stars in v_R - v_ϕ space across eight metallicity bins (increasing left to right, top to bottom) for the high- α population (top) and low- α population (bottom). The low- α stars are clearly more rotation-supported at high metallicities, while the high- α sample shows a broader velocity structure across all bins, consistent with thick-disc and halo populations.

5.3 Gaussian Mixture Model Fit

We follow the same Gaussian mixture model fitting procedure as in Section 4.1, but now separately for the high- and low- α sequences.

α -Sequence	VMP ($[M/H] < -2.0$)	IMP ($-2.0 < [M/H] < -1.3$)	MP1 ($-1.3 < [M/H] < -1.0$)	MP2 ($-1.0 < [M/H] < -0.7$)
High- α	1	4	5	3
Low- α	1	2	4	6

Table 2: Number of Gaussian Mixture components selected by the BIC for each metallicity bin, split by α -sequence.

Following the methodology described in Section 3.2, Table 2 summarises the number of components selected by the Bayesian Information Criterion (BIC) for each metallicity bin. It shows that both α -sequences are well-described by a single broad Gaussian in the very-metal-poor (VMP) bin, consistent with a pressure-supported halo. With increasing metallicity the low- α branch adds components gradually ($1 \rightarrow 2 \rightarrow 4 \rightarrow 6$), reflecting the orderly emergence of a thin-disc peak and its progressively colder tail. The high- α stars, in contrast, already require four Gaussians in the intermediate-metallicity bin (IMP) and peak at five in MP1 before contracting to three in the metal-rich MP2 interval ($-1.0 < [M/H] < -0.7$).

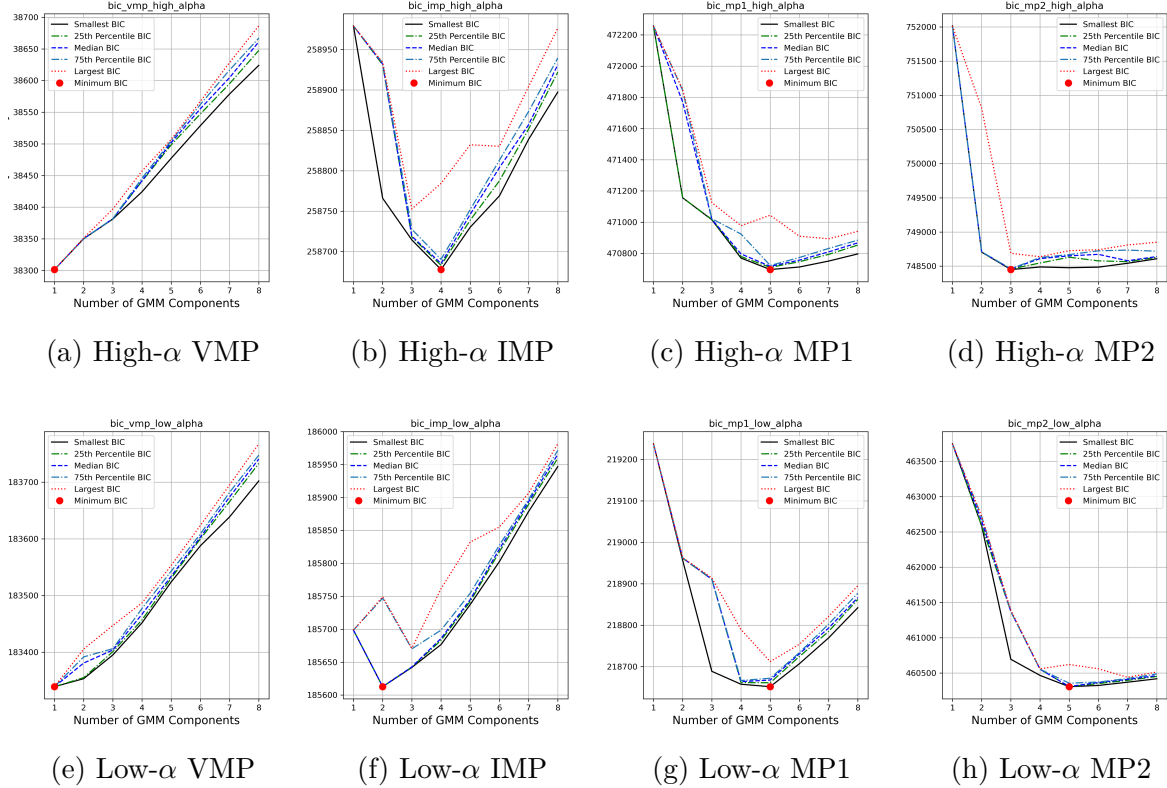


Figure 13: BIC scores for different metallicity bins, grouped by high- and low- α populations.

5.4 High alpha Gaussian Mixture Model Fit

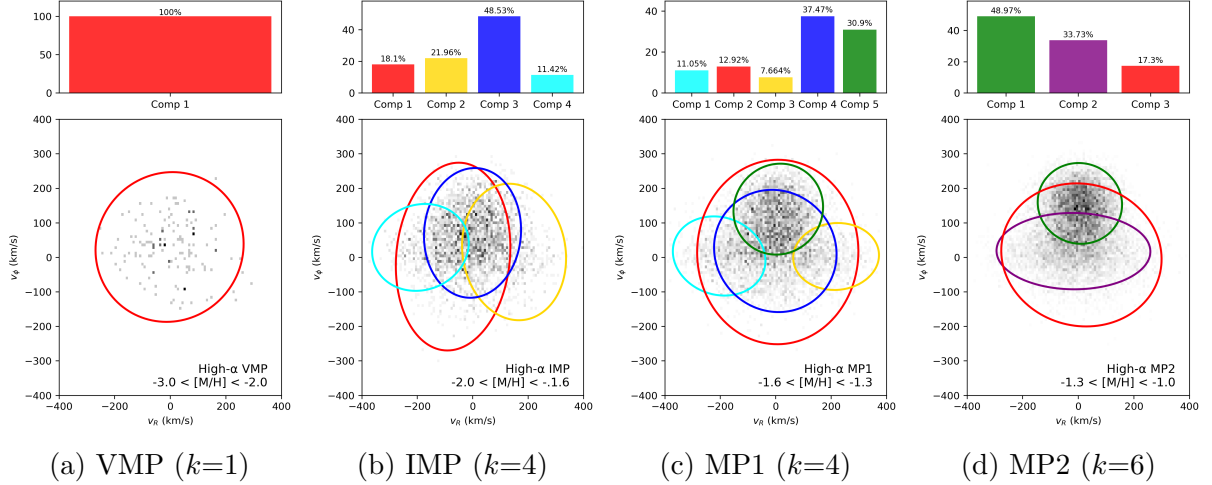


Figure 14: XD-GMM decomposition of high- α giants in four metallicity bins. Grey ellipses mark the 1σ contours of each Gaussian component.

Components	Weights (%)	v_R	σ_R	v_ϕ	σ_ϕ	v_Z	σ_Z
VMP: $-3.0 < [M/H] < -2.0$ (1033 stars)							
Stationary halo	100.0	-2.40	133.08	29.80	108.47	6.80	104.61
IMP: $-2.0 < [M/H] < -1.6$ (7050 stars)							
Stationary halo-like	18.1	-70.63	103.27	2.00	136.02	-13.00	120.01
Prograde halo-like	48.5	-0.56	87.54	70.63	93.97	-1.29	66.22
GS/E (1)	11.4	-188.39	87.12	28.59	62.94	-0.62	97.96
GS/E (2)	22.0	149.33	93.80	15.31	98.88	10.40	106.66
MP1: $-1.6 < [M/H] < -1.3$ (12899 stars)							
Stationary halo	12.9	7.52	145.38	15.28	133.61	-10.39	133.93
Prograde halo	37.5	-1.29	110.47	18.28	88.55	-3.74	71.46
GS/E (1)	11.0	-203.90	83.50	3.74	57.34	5.61	97.30
GS/E (2)	7.7	218.01	77.33	2.25	48.52	-2.09	104.19
Thick disc	30.9	9.38	80.76	139.48	65.87	5.41	69.98
MP2: $-1.3 < [M/H] < -1.0$ (20925 stars)							
Stationary halo	17.3	11.44	144.07	6.85	103.63	-6.84	105.99
GS/E	33.7	-17.25	138.25	17.80	55.30	-1.66	78.42
Thick Disk	49.0	5.87	75.82	156.06	58.51	-0.43	66.60

Table 3: GMM component weights and kinematics for the high- α sequence. Velocities are in km s^{-1} . Weights indicate the fraction of stars per metallicity bin.

5.5 Low alpha Gaussian Mixture Model Fit

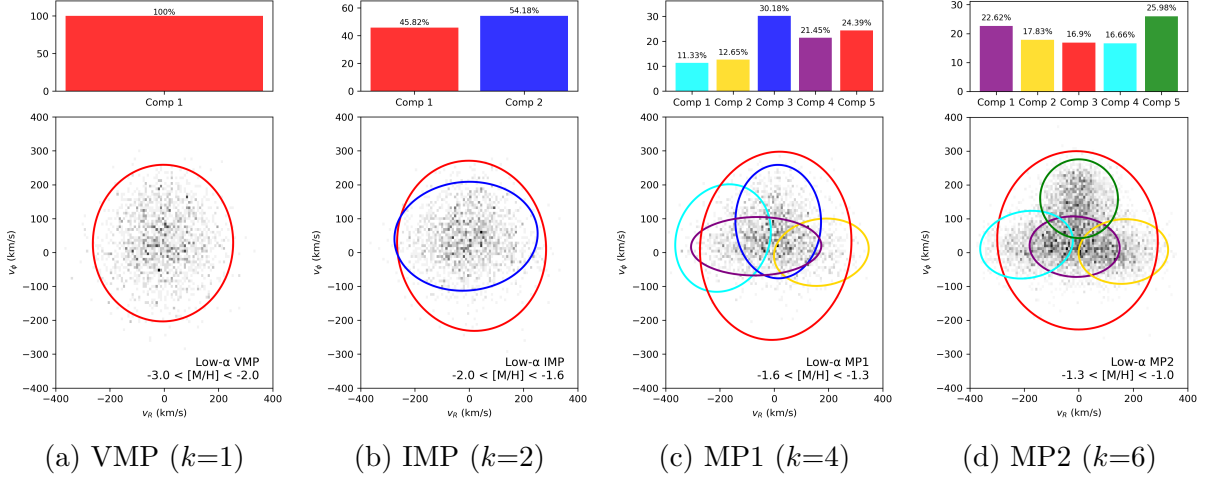


Figure 15: XD–GMM decomposition of low- α giants in four metallicity bins. Grey ellipses show the 1σ contours of every Gaussian component.

Components	Weights (%)	v_R	σ_R	v_ϕ	σ_ϕ	v_Z	σ_Z
VMP: $-3.0 < [M/H] < -2.0$ (4923 stars)							
Stationary halo	100.0	-4.62	129.15	27.66	115.57	1.01	111.32
IMP: $-2.0 < [M/H] < -1.6$ (5028 stars)							
Stationary halo	45.8	8.56	137.17	19.68	125.55	1.83	124.15
Prograde halo	54.2	-11.85	131.79	47.90	80.37	0.64	75.82
MP1: $-1.6 < [M/H] < -1.3$ (5946 stars)							
Stationary halo	24.4	5.41	139.42	19.70	138.87	2.94	135.64
Prograde halo	30.2	14.54	78.81	91.12	83.70	5.48	63.63
GS/E (1)	11.3	-188.64	87.98	42.56	79.32	-72.37	77.06
GS/E (2)	12.7	173.40	87.20	0.68	49.72	16.85	112.90
GS/E(3)	21.4	-66.55	119.92	18.41	43.14	12.37	74.31
MP2: $-1.3 < [M/H] < -1.0$ (12651 stars)							
Stationary halo	17.8	163.48	82.07	3.39	47.81	-12.64	110.72
Prograde halo	22.6	-15.34	82.64	17.65	44.68	-1.25	60.79
GS/E (1)	16.7	-191.82	85.03	23.55	50.04	2.49	104.42
GS/E (2)	16.9	-4.81	147.30	36.45	131.74	0.75	134.58
Thick disc	26.0	0.83	71.40	159.38	58.19	-1.14	55.54

Table 4: XD–GMM component weights and kinematics for the low- α sequence. Velocities are in km s^{-1} . Weights are the fractional contribution of each component.

5.6 Comparing the high and low α GMMs

The two chemical sequences reveal markedly different kinematic evolutions.

Very–metal–poor regime (VMP: $[M/H] < -2$). Both samples are modelled by a single, non–rotating halo Gaussian, confirming the absence of disc-like motions at the lowest abundances. The velocity ellipsoids are nearly isotropic ($\sigma_R:\sigma_\phi:\sigma_Z \simeq 1:1:1$), but

the high- α stars have a $\sim 10 \text{ km s}^{-1}$ smaller σ_ϕ , hinting at an early imprint of prograde stirring.

Intermediate–metallicity regime (IMP: $-2.0 < [\text{M}/\text{H}] < -1.6$). Here the low- α population already splits into stationary and prograde halo Gaussians of comparable weight (46%/54%), whereas the high- α fit is still dominated by four hot components, two of which trace the Gaia–Sausage/Enceladus debris. Thus rotation sets in earlier for α -poor stars, but remains dynamically hot.

Disc onset (MP1: $-1.6 < [\text{M}/\text{H}] < -1.3$). A thick-disc Gaussian appears in the high- α branch (31% weight, $v_\phi \sim 140 \text{ km s}^{-1}$), while the low- α mixture still requires five halo/GS/E components and shows no cold disc type structure. High- α stars therefore seem settle into a rotation-supported structure sooner.

Transition to disc dominance (MP2: $-1.3 < [\text{M}/\text{H}] < -1.0$). The high- α solution simplifies to three Gaussians: a thick disc (49%), a GS/E-like halo (34%) and a small stationary halo (17%). In contrast, the low- α fit remains complex (six Gaussians) but now includes a thick disc (26%) alongside four halo/GS/E components. We expect an ultra-cold, thin-disc Gaussian, however this is absent in this analysis due to sample selection choices.

From this analysis we infer that the high- α sequence evolves from a dispersion-supported halo to a kinematically warm thick disc between $[\text{M}/\text{H}] \simeq -1.6$ and -1.3 , whereas the low- α sequence starts to gain rotation at slightly lower metallicity yet remains halo-dominated until $[\text{M}/\text{H}] \gtrsim -1.3$. The continuing prominence of GS/E-type Gaussians in every low- α bin highlights the dynamical footprint of the last major merger on these stars, while the simpler three-component mix in the high- α /MP2 slice suggests an earlier, cleaner consolidation of the *in-situ* thick disc. Taken together, the two sequences trace the “two-phase” disc-building picture of [Haywood et al. \[2013\]](#): an early, α -rich epoch that settles into the thick disc, followed by a later, α -poor phase that assembles the thin disc from progressively enriched and dynamically cooler gas.

6 Discussion

7 problems with [Zhang et al. \[2024\]](#)

i do not believe random initial coditions are used for bic and gmm fitting in order to get results with astrophysical meaning, k means inistialisation is required this is because gmms are very senstitive to initial conditions, and can easily get stuck in local minima.

8 Extension direction

9 Conclusion

References

- D. An and T. C. Beers. A blueprint for the milky way’s stellar populations: The power of large photometric and astrometric surveys. *The Astrophysical Journal*, 897(1):39, July 2020. doi: 10.3847/1538-4357/ab8d39. URL <https://ui.adsabs.harvard.edu/abs/2020ApJ...897...39A>.
- F. Anders, P. Gispert, B. Ratcliffe, C. Chiappini, I. Minchev, S. Nepal, A. B. A. Queiroz, J. A. S. Amarante, T. Antoja, G. Casali, L. Casamiquela, A. Khalatyan, A. Miglio, H. Perottoni, and M. Schultheis. Spectroscopic age estimates for apogee red-giant stars: Precise spatial and kinematic trends with age in the galactic disc. *Astronomy and Astrophysics*, 678:A158, Oct. 2023. ISSN 1432-0746. doi: 10.1051/0004-6361/202346666. URL <http://dx.doi.org/10.1051/0004-6361/202346666>.
- R. Andrae, H.-W. Rix, and V. Chandra. Robust data-driven metallicities for 175 million stars from gaia xp spectra. *The Astrophysical Journal Supplement Series*, 267(1):8, jul 2023. doi: 10.3847/1538-4365/acd53e. URL <https://dx.doi.org/10.3847/1538-4365/acd53e>.
- A. Arentsen, E. Starkenburg, N. F. Martin, D. S. Aguado, D. B. Zucker, C. Allende Prieto, V. Hill, K. A. Venn, R. G. Carlberg, J. I. González Hernández, L. I. Mashonkina, J. F. Navarro, R. Sánchez-Janssen, M. Schultheis, G. F. Thomas, K. Youakim, G. F. Lewis, J. D. Simpson, Z. Wan, R. E. Cohen, D. Geisler, and J. E. O’Connell. The pristine inner galaxy survey (pigs) ii: Uncovering the most metal-poor populations in the inner milky way. *Monthly Notices of the Royal Astronomical Society*, 496(4):4964–4978, July 2020a. ISSN 1365-2966. doi: 10.1093/mnras/staa1661. URL <http://dx.doi.org/10.1093/mnras/staa1661>.
- A. Arentsen, E. Starkenburg, N. F. Martin, V. Hill, R. Ibata, A. Kunder, M. Schultheis, K. A. Venn, D. B. Zucker, D. Aguado, R. Carlberg, J. I. González Hernández, C. Lardo, N. Longeard, K. Malhan, J. F. Navarro, R. Sánchez-Janssen, F. Sestito, G. Thomas, K. Youakim, G. F. Lewis, J. D. Simpson, and Z. Wan. The pristine inner galaxy survey (pigs) i: Tracing the kinematics of metal-poor stars in the galactic bulge. *Monthly Notices of the Royal Astronomical Society*, 491(1):L11–L16, January 2020b. doi: 10.1093/mnrasl/slz156. URL <https://ui.adsabs.harvard.edu/abs/2020MNRAS.491L.11A>.
- C. A. L. Bailer-Jones, J. Rybizki, M. Fouesneau, M. Demleitner, and R. Andrae. VizieR Online Data Catalog: Distances to 1.47 billion stars in Gaia EDR3 (Bailer-Jones+, 2021). VizieR On-line Data Catalog: I/352. Originally published in: 2021AJ....161..147B, Feb. 2021.
- V. Belokurov and A. Kravtsov. From dawn till disc: Milky way’s turbulent youth revealed by the apogee+gaia data. *Monthly Notices of the Royal Astronomical Society*, 514(1):689–714, May 2022. ISSN 1365-2966. doi: 10.1093/mnras/stac1267. URL <http://dx.doi.org/10.1093/mnras/stac1267>.
- V. Belokurov, D. Erkal, N. W. Evans, S. E. Koposov, and A. J. Deason. Co-formation of the disc and the stellar halo. *Monthly Notices of the Royal Astronomical Society*, 478(1):611–619, June 2018. ISSN 1365-2966. doi: 10.1093/mnras/sty982. URL <http://dx.doi.org/10.1093/mnras/sty982>.

- V. Belokurov, J. L. Sanders, A. Fattahi, M. C. Smith, A. J. Deason, N. W. Evans, and R. J. J. Grand. The biggest splash. *Monthly Notices of the Royal Astronomical Society*, 494(3):3880–3898, Apr. 2020. ISSN 1365-2966. doi: 10.1093/mnras/staa876. URL <http://dx.doi.org/10.1093/mnras/staa876>.
- S. A. Bird, X.-X. Xue, C. Liu, J. Shen, C. Flynn, C. Yang, G. Zhao, and H.-J. Tian. Constraints on the assembly history of the milky way’s smooth, diffuse stellar halo from the metallicity-dependent, radially dominated velocity anisotropy profiles probed with k giants and bhb stars using lamost, sdss/segue, and gaia. *The Astrophysical Journal*, 919(1):66, Sept. 2021. ISSN 1538-4357. doi: 10.3847/1538-4357/abfa9e. URL <http://dx.doi.org/10.3847/1538-4357/abfa9e>.
- J. Bland-Hawthorn and O. Gerhard. The galaxy in context: Structural, kinematic, and integrated properties. *Annual Review of Astronomy and Astrophysics*, 54(1):529–596, Sept. 2016. ISSN 1545-4282. doi: 10.1146/annurev-astro-081915-023441. URL <http://dx.doi.org/10.1146/annurev-astro-081915-023441>.
- J. Bovy, D. W. Hogg, and S. T. Roweis. Extreme deconvolution: Inferring complete distribution functions from noisy, heterogeneous and incomplete observations. *The Annals of Applied Statistics*, 5(2B), June 2011. ISSN 1932-6157. doi: 10.1214/10-aoas439. URL <http://dx.doi.org/10.1214/10-AOAS439>.
- J. S. Bullock and M. Boylan-Kolchin. Small-scale challenges to the lambda cdm paradigm. *Annual Review of Astronomy and Astrophysics*, 55(1):343–387, Aug. 2017. ISSN 1545-4282. doi: 10.1146/annurev-astro-091916-055313. URL <http://dx.doi.org/10.1146/annurev-astro-091916-055313>.
- D. Carollo, M. Chiba, M. Ishigaki, K. Freeman, T. C. Beers, Y. S. Lee, P. Tissera, C. Battistini, and F. Primas. Evidence for the third stellar population in the milky way’s disk. *The Astrophysical Journal*, 887(1):22, December 2019. doi: 10.3847/1538-4357/ab517c. URL <https://ui.adsabs.harvard.edu/abs/2019ApJ...887...22C>.
- V. Chandra, V. A. Semenov, H.-W. Rix, C. Conroy, A. Bonaca, R. P. Naidu, R. Andrae, J. Li, and L. Hernquist. The three-phase evolution of the milky way. *The Astrophysical Journal*, 972(1):112, Aug. 2024. ISSN 1538-4357. doi: 10.3847/1538-4357/ad5b60. URL <http://dx.doi.org/10.3847/1538-4357/ad5b60>.
- M. Chiba and T. C. Beers. Kinematics of metal-poor stars in the galaxy. iii. formation of the stellar halo and thick disk as revealed from a large sample of nonkinematically selected stars. *The Astronomical Journal*, 119(6):2843–2865, June 2000. ISSN 0004-6256. doi: 10.1086/301409. URL <http://dx.doi.org/10.1086/301409>.
- A. P. Cooper, S. Cole, C. S. Frenk, S. D. M. White, J. Helly, A. J. Benson, G. De Lucia, A. Helmi, A. Jenkins, J. F. Navarro, V. Springel, and J. Wang. Galactic stellar haloes in the cdm model: Galactic stellar haloes in the cdm model. *Monthly Notices of the Royal Astronomical Society*, 406(2):744–766, May 2010. ISSN 0035-8711. doi: 10.1111/j.1365-2966.2010.16740.x. URL <http://dx.doi.org/10.1111/j.1365-2966.2010.16740.x>.
- G. Cordini, G. S. Da Costa, D. Yong, A. D. Mackey, A. F. Marino, S. Monty, T. Nordlander, J. E. Norris, M. Asplund, M. S. Bessell, A. R. Casey, A. Frebel, K. Lind, S. J. Murphy, B. P. Schmidt, X. D. Gao, T. Xylakis-Dornbusch, A. M. Amarsi,

- and A. P. Milone. Exploring the galaxy’s halo and very metal-weak thick disc with skymapper and gaia dr2. *Monthly Notices of the Royal Astronomical Society*, 503(2):2539–2561, Nov. 2020. ISSN 1365-2966. doi: 10.1093/mnras/staa3417. URL <http://dx.doi.org/10.1093/mnras/staa3417>.
- P. Di Matteo, M. Haywood, M. D. Lehnert, D. Katz, S. Khoperskov, O. N. Snaith, A. Gomez, and N. Robichon. The milky way has no in-situ halo other than the heated thick disc: Composition of the stellar halo and age-dating the last significant merger with gaia dr2 and apogee. *Astronomy & Astrophysics*, 632:A4, Nov. 2019. ISSN 1432-0746. doi: 10.1051/0004-6361/201834929. URL <http://dx.doi.org/10.1051/0004-6361/201834929>.
- A. M. Dillamore, V. Belokurov, N. W. Evans, and E. Y. Davies. Stellar halo substructure generated by bar resonances. *Monthly Notices of the Royal Astronomical Society*, 524(3):3596–3608, July 2023. ISSN 1365-2966. doi: 10.1093/mnras/stad2136. URL <http://dx.doi.org/10.1093/mnras/stad2136>.
- S. M. Fall and R. Chandar. Similarities in populations of star clusters. *The Astrophysical Journal*, 752(2):96, may 2012. doi: 10.1088/0004-637X/752/2/96. URL <https://dx.doi.org/10.1088/0004-637X/752/2/96>.
- Gaia Collaboration, A. Vallenari, A. G. A. Brown, et al. Gaia data release 3: Summary of the content and survey properties. *Astronomy & Astrophysics*, 674:A1, 2023. doi: 10.1051/0004-6361/202243940.
- C. Gallart, E. J. Bernard, C. B. Brook, T. Ruiz-Lara, S. Cassisi, V. Hill, and M. Monelli. Uncovering the birth of the milky way through accurate stellar ages with gaia. *Nature Astronomy*, 3(10):932–939, July 2019. ISSN 2397-3366. doi: 10.1038/s41550-019-0829-5. URL <http://dx.doi.org/10.1038/s41550-019-0829-5>.
- G. M. Green. dustmaps: A python interface for maps of interstellar dust. *Journal of Open Source Software*, 3(26):695, 2018. doi: 10.21105/joss.00695. URL <https://doi.org/10.21105/joss.00695>.
- A. B. Gurvich, J. Stern, C.-A. Faucher-Giguère, P. F. Hopkins, A. Wetzel, J. Moreno, C. C. Hayward, A. J. Richings, and Z. Hafen. Rapid disc settling and the transition from bursty to steady star formation in milky way-mass galaxies. *Monthly Notices of the Royal Astronomical Society*, 519(2):2598–2614, February 2023. doi: 10.1093/mnras/stac3712. URL <https://ui.adsabs.harvard.edu/abs/2023MNRAS.519.2598G>.
- M. Haywood, P. Di Matteo, M. D. Lehnert, D. Katz, and A. Gómez. The age structure of stellar populations in the solar vicinity: Clues of a two-phase formation history of the milky way disk. *Astronomy and Astrophysics*, 560:A109, Dec. 2013. ISSN 1432-0746. doi: 10.1051/0004-6361/201321397. URL <http://dx.doi.org/10.1051/0004-6361/201321397>.
- A. Helmi. Streams, substructures, and the early history of the milky way. *Annual Review of Astronomy and Astrophysics*, 58(1):205–256, Aug. 2020. ISSN 1545-4282. doi: 10.1146/annurev-astro-032620-021917. URL <http://dx.doi.org/10.1146/annurev-astro-032620-021917>.
- A. Helmi and P. Tim de Zeeuw. Mapping the substructure in the galactic halo with the

- next generation of astrometric satellites. *Monthly Notices of the Royal Astronomical Society*, 319(3):657–665, 2000.
- A. Helmi, C. Babusiaux, H. H. Koppelman, D. Massari, J. Veljanoski, and A. G. A. Brown. The merger that led to the formation of the milky way’s inner stellar halo and thick disk. *Nature*, 563(7729):85–88, Oct. 2018. ISSN 1476-4687. doi: 10.1038/s41586-018-0625-x. URL <http://dx.doi.org/10.1038/s41586-018-0625-x>.
- L. Lancaster, S. E. Koposov, V. Belokurov, N. W. Evans, and A. J. Deason. The halo’s ancient metal-rich progenitor revealed with bhb stars. *Monthly Notices of the Royal Astronomical Society*, 486(1):378–389, Mar. 2019. ISSN 1365-2966. doi: 10.1093/mnras/stz853. URL <http://dx.doi.org/10.1093/mnras/stz853>.
- H. W. Leung and J. Bovy. Deep learning of multi-element abundances from high-resolution spectroscopic data. *Monthly Notices of the Royal Astronomical Society*, 483(3):3255–3277, 2019.
- J. Li, K. W. K. Wong, D. W. Hogg, H.-W. Rix, and V. Chandra. Aspgap: Augmented stellar parameters and abundances for 23 million rgb stars from gaia xp low-resolution spectra, 2023. URL <https://arxiv.org/abs/2309.14294>.
- M. K. Mardini, A. Frebel, A. Chiti, Y. Meiron, K. V. Brauer, and X. Ou. The atari disk, a metal-poor stellar population in the disk system of the milky way. *The Astrophysical Journal*, 936(1):78, Sept. 2022. ISSN 1538-4357. doi: 10.3847/1538-4357/ac8102. URL <http://dx.doi.org/10.3847/1538-4357/ac8102>.
- P. J. McMillan. The mass distribution and gravitational potential of the milky way. *Monthly Notices of the Royal Astronomical Society*, 465(1):76–94, Oct. 2016. ISSN 1365-2966. doi: 10.1093/mnras/stw2759. URL <http://dx.doi.org/10.1093/mnras/stw2759>.
- P. Melchior and A. Goulding. Filling the gaps: Gaussian mixture models from noisy, truncated or incomplete samples. *Astronomy and Computing*, 25, 11 2016. doi: 10.1016/j.ascom.2018.09.013.
- B. Nordström, M. Mayor, J. Andersen, J. Holmberg, F. Pont, B. R. Jørgensen, E. H. Olsen, S. Udry, and N. Mowlavi. The geneva-copenhagen survey of the solar neighbourhood: Ages, metallicities, and kinematic properties of \sim 14 000 f and g dwarfs. *Astronomy and Astrophysics*, 418(3):989–1019, Apr. 2004. ISSN 1432-0746. doi: 10.1051/0004-6361:20035959. URL <http://dx.doi.org/10.1051/0004-6361:20035959>.
- J. Norris, M. S. Bessell, and A. J. Pickles. Population studies. i. the bidelman-macconnell “weak-metal” stars. *The Astrophysical Journal Supplement Series*, 58:463–492, July 1985. doi: 10.1086/191049. URL <https://ui.adsabs.harvard.edu/abs/1985ApJS..58..463N>.
- A. B. Pace. The Local Volume Database: a library of the observed properties of nearby dwarf galaxies and star clusters. *arXiv e-prints*, art. arXiv:2411.07424, Nov. 2024. doi: 10.48550/arXiv.2411.07424.
- C. W. Purcell, J. S. Bullock, and A. R. Zentner. Shredded galaxies as the source of diffuse

- intrahalo light on varying scales. *The Astrophysical Journal*, 666(1):20–33, Sept. 2007. ISSN 1538-4357. doi: 10.1086/519787. URL <http://dx.doi.org/10.1086/519787>.
- H.-W. Rix, V. Chandra, R. Andrae, A. M. Price-Whelan, D. H. Weinberg, C. Conroy, M. Fouesneau, D. W. Hogg, F. De Angeli, R. P. Naidu, M. Xiang, and D. Ruz-Mieres. The poor old heart of the milky way. *The Astrophysical Journal*, 941(1):45, Dec. 2022. ISSN 1538-4357. doi: 10.3847/1538-4357/ac9e01. URL <http://dx.doi.org/10.3847/1538-4357/ac9e01>.
- I. B. Santistevan, A. Wetzel, R. E. Sanderson, K. El-Badry, J. Samuel, and C.-A. Faucher-Giguère. The origin of metal-poor stars on prograde disc orbits in fire simulations of milky way-mass galaxies. *Monthly Notices of the Royal Astronomical Society*, 505(1):921–938, July 2021. doi: 10.1093/mnras/stab1345. URL <https://ui.adsabs.harvard.edu/abs/2021MNRAS.505..921S>.
- G. Schwarz. Estimating the dimension of a model. *The Annals of Statistics*, 6(2):461–464, 1978. ISSN 00905364, 21688966. URL <http://www.jstor.org/stable/2958889>.
- R. Schönrich, J. Binney, and W. Dehnen. Local kinematics and the local standard of rest. *Monthly Notices of the Royal Astronomical Society*, 403(4):1829–1833, Apr. 2010. ISSN 1365-2966. doi: 10.1111/j.1365-2966.2010.16253.x. URL <http://dx.doi.org/10.1111/j.1365-2966.2010.16253.x>.
- F. Sestito, N. Martin, and E. Starkenburg. Tracing the formation of the milky way through ultra metal-poor stars. In *The Gaia Universe*, page 47, Apr. 2019. doi: 10.5281/zenodo.3236051.
- F. Sestito, T. Buck, E. Starkenburg, N. F. Martin, J. F. Navarro, K. A. Venn, A. Obreja, P. Jablonka, and A. V. Macciò. Exploring the origin of low-metallicity stars in milky-way-like galaxies with the nihao-uhd simulations. *Monthly Notices of the Royal Astronomical Society*, 500(3):3750–3762, Nov. 2020. ISSN 1365-2966. doi: 10.1093/mnras/staa3479. URL <http://dx.doi.org/10.1093/mnras/staa3479>.
- R. Tkachenko, K. Vieira, A. Lutsenko, V. Korchagin, and G. Carraro. Determining the scale length and height of the milky way’s thick disc using rr lyrae. *Universe*, 11(4):132, apr 2025. doi: 10.3390/universe11040132. URL <http://dx.doi.org/10.3390/universe11040132>.
- K. A. Venn, C. L. Kielty, F. Sestito, E. Starkenburg, N. Martin, D. S. Aguado, A. Aréntsen, P. Bonifacio, E. Caffau, V. Hill, P. Jablonka, C. Lardo, L. Mashonkina, J. F. Navarro, C. Sneden, G. Thomas, K. Youakim, J. I. González-Hernández, R. S. Janssen, R. Carlberg, and K. Malhan. The pristine survey - ix. cfht espadons spectroscopic analysis of 115 bright metal-poor candidate stars. *Monthly Notices of the Royal Astronomical Society*, 492(3):3241–3262, Mar. 2020. doi: 10.1093/mnras/stz3546.
- A. Viswanathan, D. Horta, A. M. Price-Whelan, and E. Starkenburg. A slow spin to win – the gradual evolution of the proto-galaxy to the old disc, 2024. URL <https://arxiv.org/abs/2411.12165>.
- H. Zhang, A. Ardern-Arentsen, and V. Belokurov. On the existence of a very metal-poor disc in the milky way, 2024. URL <https://arxiv.org/abs/2311.09294>.